Search for Black Holes and Sphalerons Using Novel Machine Learning Techniques at CMS

Tamas Almos Vami[1]* and Danyi Zhang[1] for the CMS Collaboration

[1]*Department of Physics, University of California Santa Barbara, Santa Barbara, CA 93106, USA*

Abstract

A comprehensive search for microscopic black holes and electroweak sphalerons is presented, using proton-proton collision data collected by the CMS detector during 2016–2018, corresponding to an integrated luminosity of 138 fb^{-1}. A novel tool has been developed to identify collider events with distinct kinematic features, based on the phase space distance between events. In the context of models with large extra dimensions, semiclassical black holes with masses below 9.0-11.4 TeV are excluded by this search, significantly extending previous sensitivity. Additionally, a dedicated search for electroweak sphaleron transitions has been performed. An upper limit of 0.0025 is set at 95% confidence level on the fraction of quark-quark interactions with center-of-mass energy above the nominal threshold of 9 TeV that result in sphaleron transitions.

Keywords: pp collisions, Beyond standard model, Black holes and sphalerons, Phase space distance, Machine learning
DOI: 10.31526/PHEP.2026.21

1. BLACK HOLES AT CMS?

Usually, discussions about black holes (BHs) concern cosmic scales involving enormous masses and volumes. However, the criterion for black hole formation is rather simple: the object must be smaller than its Schwarzschild radius. The Schwarzschild radius for an object with mass M is given in Eq. 1, where G is the gravitational constant and c is the speed of light [1]:

$$R_S = \frac{2GM}{c^2} \tag{1}$$

If we calculate the radius for the Earth, $R_S(M = M_{\text{Earth}})$, we find that compressing our planet to a few millimeters would be enough for it to become a black hole.

The Large Hadron Collider (LHC) at CERN collides proton beams with the center-of-mass energy of 13 TeV. One could ask the question: within what radius would this energy need to be confined to form a black hole? Following the same calculation, we find that $R_S(M = 13\ \text{TeV}) \approx 10^{-50}$ m. That is an absurdly small scale: for comparison, the Planck lengths, which is the natural quantum-gravity length scale, is $l_{\text{Planck}} \approx 10^{-35}$ m. Thus, we can conclude that the LHC cannot produce black holes, assuming no new physics beyond the Standard Model (SM).

However, if our world has more than $3+1$ dimensions [2, 3, 4, 5, 6], denoting the extra dimensions with n, the Schwarzschild radius calculation changes as described in Eq. 2, where M_{BH} is the mass of the black hole, M_D is the Planck scale in n dimensions, and $\Omega_{n+2} = (2\pi)^{\frac{n+3}{2}}/\Gamma(\frac{n+3}{2})$.

$$R'_S = \left[\frac{16\pi}{(n+2)\Omega_{n+2}}\frac{M_{BH}}{M_D^{n+2}}\right]^{\frac{1}{n+1}} \tag{2}$$

With this modification, the $R'_S(M = 13\ \text{TeV}) \approx 10^{-20}$ m for representative choices of M_D and n. Based on the Heisenberg uncertainty, $\Delta x = \hbar c/13\ \text{TeV} \approx 10^{-20}$ m, the extra-dimensional microscopic black holes are within the LHC reach [7, 8, 9].

However, even if the LHC could produce such objects, they would undergo Hawking radiation. The time τ it takes to evaporate a black hole is proportional to the cube of its mass, $\tau \propto M^3$. So a microscopic black hole at the LHC will immediately decay to high multiplicity, high energy and isotropic objects. The CMS experiment [10] will thus reconstruct these as jets, leptons, and missing momentum, as illustrated in Figure: 1. Isotropic events like these are really hard to separate from high-multiplicity SM events, so distinguishing them requires innovative techniques and machine learning tools. The results presented in this work are documented in CMS as `CMS-PAS-EXO-24-028` [11].

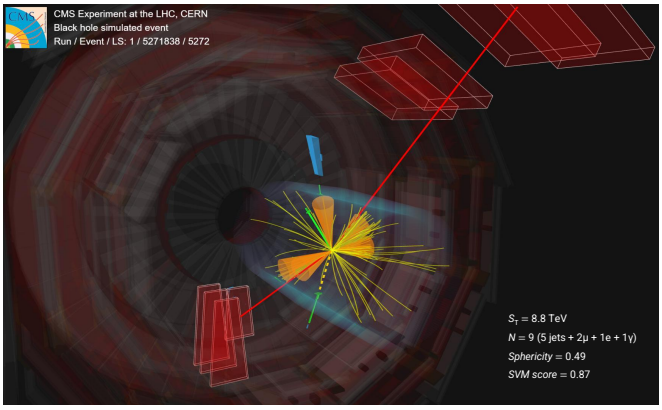

FIGURE 1: Event display of the final products from a simulated microscopic black hole evaporation at the LHC. The red lines represent muons, the orange cones are jets, the yellow lines are tracks, the green line is an electron, and the blue block is for a photon interaction in the electric calorimeter.

*Corresponding author: Tamas.Almos.Vami@cern.ch

2. WHAT ARE SPHALERONS?

Sphalerons are unstable, finite-energy saddle-point configurations of the electroweak theory that interpolate between topologically distinct gauge vacua characterized by different Chern–Simons number N_{CS} [12, 13]. The cross section for such processes is expected to be proportional to a model-dependent pre-exponential factor [14, 15, 16, 17]. The Chern–Simons number N_{CS} labels the distinct vacua, while the sphaleron energy E_{sph} corresponds to the height of the potential barrier separating neighboring vacua.

A sphaleron transition corresponds to a change in vacuum configuration, i.e., a shift in the N_{CS}. We denote the probability of a $\Delta N_{CS} = 1$ change with $p(N_{CS})$. We consider events with $p(N_{CS})$ values of 0%, 50% and 100%. The meaning of 50% is that half of the events have $\Delta N_{CS} = -1$ while the other half have $\Delta N_{CS} = 1$. In these processes, baryon (B) and lepton (L) number conservation is violated while the B-L is conserved. In ΔN_{CS} of (-)1 processes all left-handed (anti-)fermions from each SM family are created. This mechanism can explain the matter-antimatter asymmetry problem. The final products are similar to the BH evaporation products, displayed in Figure: 2; thus, the same analysis techniques can be applied.

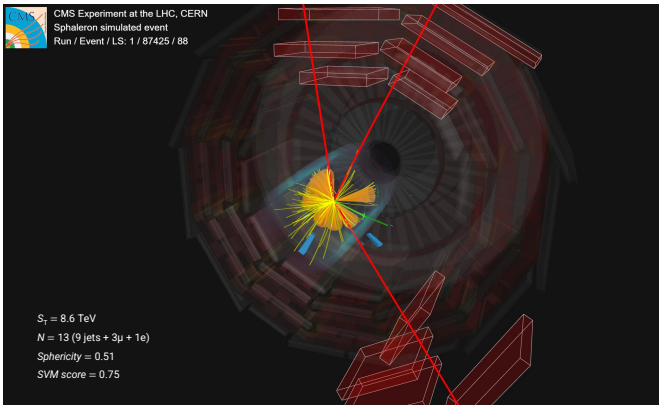

FIGURE 2: Event display of the final products from a simulated sphaleron process at the LHC.

3. SIMULATED SAMPLES

We produced black hole signal samples under different assumptions regarding their angular momentum, energy loss, and decay mechanisms. We generated samples labeled with `B` using the BLACKMAX [18] generator: `B1` corresponds to nonrotating black holes, `B2` to rotating ones without graviton emission, and `B3` to rotating black holes that include energy and momentum loss. We also generated samples labeled with `C` using the CHARYBDIS2 [19, 20] generator: `C1` represents rotating black holes, `C2` nonrotating ones, `C3` rotating black holes with the evaporation model described in [21, 22], `C4` rotating ones with the Yoshino–Rychkov (YR) model [23], which provides a conservative bound incorporating impact parameter effects, `C5` rotating black holes with a stable remnant model [24, 25, 26], where the remnant is a colorless object akin to a quark–antiquark bound state, and `C6` nonrotating black holes with a boiling remnant model [27, 28], in which the remnant continues to evaporate until the Hawking temperature reaches a maximum value equal to M_D.

We used the BARYOGEN [29] generator to simulate sphaleron processes. This generator neglects the gauge bosons and thus represents the conservative choice.

To guide the selection criteria and train machine learning models, we simulated four-flavor Quantum Chromodynamics (QCD) multijet production with MADGRAPH [30] at leading order using the MLM matching scheme [31] with `CP5` tunes[32].

4. NOVEL DATA REPRESENTATION

In [33], the authors proposed that a collision event can be represented on the phase space manifold Π_N of the scattering amplitudes for the N objects (jets, photons, and leptons) in the event. It can be expressed as the product of an $(N-1)$-simplex Δ_{N-1} and a $(2N-3)$-dimensional hypersphere S_{2N-3}, i.e., $\Pi_N \cong \Delta_{N-1} \times S_{2N-3}$. For this study, we set $N = 30$ and in case there are fewer objects in the event, we assign zero values to them (called zero-padding). Next, explicit global coordinates of the phase space were introduced, denoted by $\vec{\rho}$ for the simplex and $\vec{v}$ for the hypersphere. Using these coordinates, one can define a distance between two events, A and B, denoted as $d_\Pi(\vec{\rho}_A, \vec{v}'_A; \vec{\rho}_B, \vec{v}'_B)$ and expressed in Eq. 3, where d_Δ is the distance on the simplex, d_S is the distance on the hypersphere, c serves as a reweighting factor that gives rise to equally valid phase space distances, $\alpha = \frac{1}{16\pi^2}\left(\frac{c}{4}\right)^{\frac{3-2N}{3N-4}}$ and $\beta = \frac{1}{4\pi^2}\left(\frac{c}{4}\right)^{\frac{N-1}{3N-4}}$. For further details of this metric calculation, we refer to [34].

$$d_\Pi(\vec{\rho}_A, \vec{v}'_A; \vec{\rho}_B, \vec{v}'_B) = \sqrt{\alpha\, d_\Delta^2(\vec{\rho}_A, \vec{\rho}_B) + \beta\, d_S^2(\vec{v}'_A, \vec{v}'_B)} \quad (3)$$

We calculated the pairwise distance between 10,000 events from a mixture of BH mass points with the `B1` model assuming $n = 2$ as signal, and the QCD multijet sample as background. This is displayed as a two-by-two matrix of 10,000 points in each block in Figure: 3. The distance of an event to itself is small, as expected, but nonzero because of the zero-padding. While we can see that background-to-background comparisons yield smaller distances, generally it is really hard for humans to discriminate background versus signal based on this figure.

5. MACHINE LEARNING TOOLS

To overcome the challenges of interpreting high-dimensional data, we employ advanced machine learning techniques. Specifically, we used a Support Vector Machine (SVM) [35], which is a distance-based tool that finds the optimal hyperplane to classify the signal from the background. Since our input representation is inherently geometric, the SVM provides a natural and interpretable choice. The output of the SVM is a probability of how signal-like a given event is, calibrated using the Platt scaling[36]. The distribution of the SVM score is displayed in Figure: 4. We optimized the selection criteria on this variable using the Punzi figure of merit [37]; and found that a single global selection value at 0.63 is sufficient for all mass points, and certainly simplifies the analysis. Varying this threshold between 0.5 and 0.7 changes the signal yield by only 4–25%, depending on M_{BH}. Unlike other ML approaches, here the input is a physically meaningful distance measure, making the results more interpretable than those from, for example, a neural network.

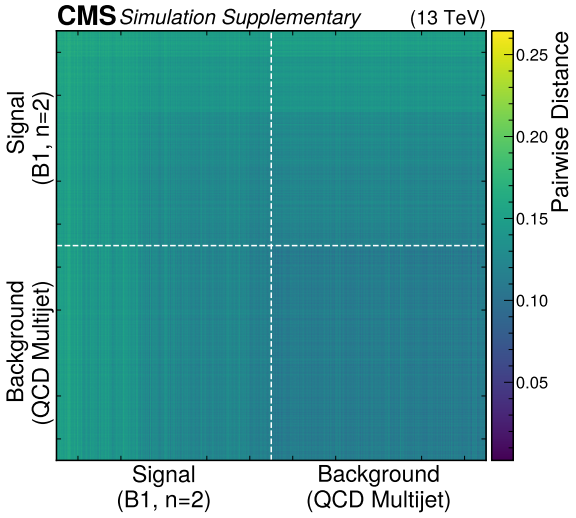

FIGURE 3: Pairwise distance between 10,000 events in each category of signal (BH with mixture mass points) and background (QCD multijets).

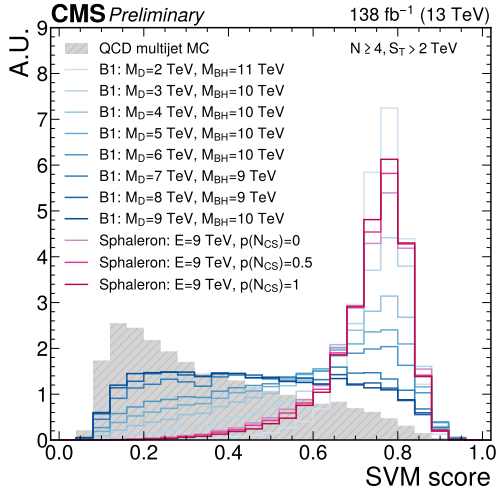

FIGURE 4: SVM score distributions for simulated QCD multijets and selected black hole (with $n = 2$) and sphaleron models.

6. FURTHER OBSERVABLES

We require all reconstructed objects to pass standard quality criteria and to have a transverse momentum p_T of at least 70 GeV. The number of objects after these selections is denoted with N, and for the final results, we consider only events by $N > 3$

Since signal events are expected to be highly spherical, we also used sphericity as a selection variable. Sphericity is calculated as shown in Eq. 4.

$$S = \frac{2\lambda_2}{\lambda_2 + \lambda_1}, \tag{4}$$

where λ_1 and λ_2 are the eigenvalues of the transverse momentum tensor S^L_{xy}, as defined in Eq. 5,

$$S^L_{xy} = \frac{1}{\sum_i p_{T,i}} \sum_i \frac{1}{p_{T,i}} \begin{bmatrix} p^2_{x,i} & p_{x,i}p_{y,i} \\ p_{x,i}p_{y,i} & p^2_{y,i} \end{bmatrix}, \tag{5}$$

where the index i extends over all objects used in the analysis. We require all events to have $S > 0.1$.

Another important variable is the scalar sum of the p_T of the objects used in the analysis, including the missing transverse momentum. It is calculated as shown in Eq. 6.

$$S_T = \left(\sum_{i=1}^{N} p_{T,i} \right) + p_T^{\text{miss}}, \tag{6}$$

After requiring the sphericity selection, the SVM score versus S_T distributions are shown in Figure: 5 for simulated QCD multijet background (left) and a selected black hole signal with $M_D = 2$ TeV, $M_{BH} = 10$ TeV and $n = 2$ (right). A similarly great signal to background discrimination can be observed for all models.

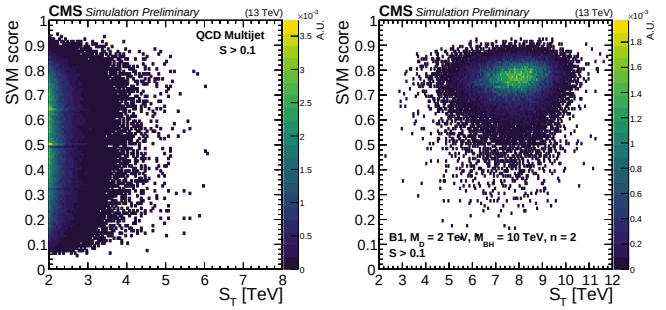

FIGURE 5: The SVM score versus the S_T distributions for simulated background (left) and a selected black hole signal model (right).

7. BACKGROUND PREDICTION

To avoid relying on the precise modeling of the high S_T tails in the QCD simulations, we use a data-driven background prediction technique. We separate the data to a FAIL and PASS region, defined by the SVM score selection at 0.63, and perform a shape based analysis using the S_T variable. We bin the S_T distribution and fit in both regions simultaneously. We then calculate the predicted yields in the PASS region using Eq. 7, where we model the PASS-FAIL ratio, $R_{\text{P/F}}(j)$ as an exponential function, and j denotes the bin index.

$$N^{\text{bkg}}_{\text{PASS}}(j) = R_{\text{P/F}}(j)\, N^{\text{bkg}}_{\text{FAIL}}(j) \tag{7}$$

We tested this method in a validation region, where we inverted the selection on the sphericity ($S < 0.1$), while keeping the other requirements the same. The prediction in this validation region shows good performance: the pulls between the data and prediction are centered at zero and have symmetric deviations. The search is statistically limited, with systematic uncertainties contributing at the few-percent level.

Figure 6 shows the post-fit S_T distributions in the FAIL (left) and PASS (right) regions, together with two selected signal simulations with red and blue curves. The gray shaded area shows

the statistical and systematic uncertainties on the background prediction. We do not observe any significant excess or deficit.

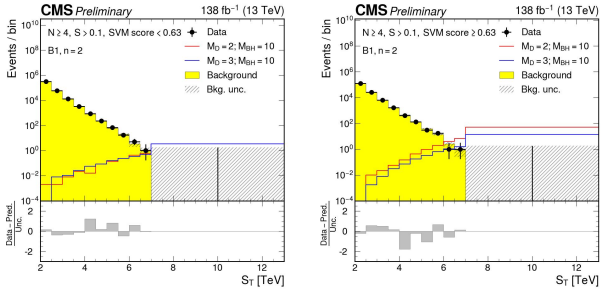

FIGURE 6: Post-fit S_T distributions in the FAIL (left) and PASS (right) regions. The red and blue curves represent two selected B1 signal examples as noted in the legend. The gray hatched area shows the statistical and systematic uncertainties on the background prediction.

8. RESULTS

Given that we did not observe any excess or deficit, we set model-dependent 95% CL asymptotic limits on signal cross section of the BH models considered. As an example, Figure: 7 shows the expected and observed 95% CL upper limits for B1 models with $M_D = 2$ TeV. The theoretical cross section is displayed with the blue curve, which includes the latest recommended parton distribution functions, NNPDF3.1 [38]. The expected and observed excluded M_{BH} is at 11.4 TeV.

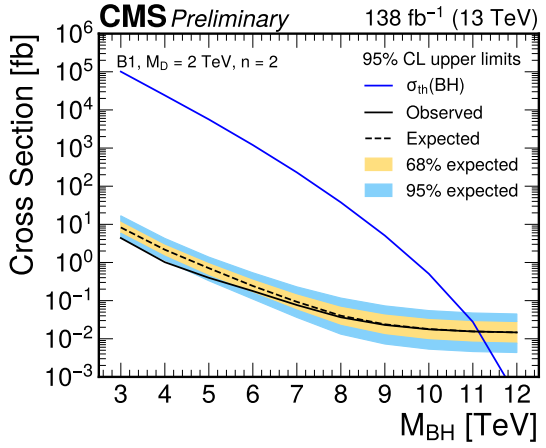

FIGURE 7: Expected and observed 95% CL upper limits for B1 models with $M_D = 2$ TeV. The blue curves represent the theoretical cross section values.

Following the same procedure, we can create a summary plot that shows the observed excluded M_{BH} as a function of the M_D. Figure 8 shows these summary plots, in the left, we see the models with BLACKMAX, and in the right the models with CHARYBDIS2. Different extra dimension values are denoted with solid, dashed, and dash-dot styles for the curves. The colors represent the different assumptions regarding angular momentum, energy-loss, and the evaporation model.

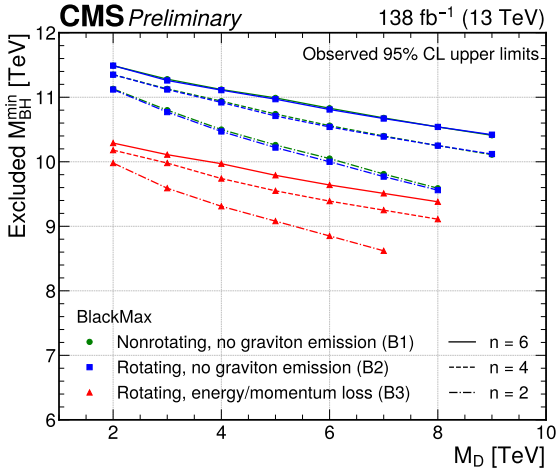

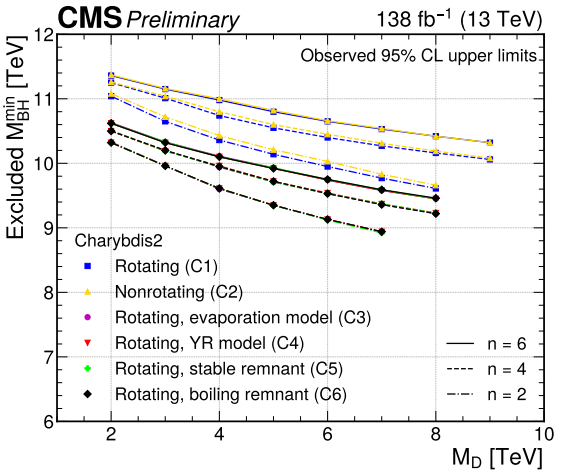

FIGURE 8: Excluded M_{BH} values as a function of M_D and n for a variety of BLACKMAX (left) and CHARYBDIS2 (right) BH models.

One can look at these results as an exclusion of the allowed number of extra dimensions as well. Figure 9 shows the maximum number of excluded extra dimensions as a function of M_D, M_{BH} values for the BLACKMAX models. The results for CHARYBDIS2 models are very similar. These results show that for the majority of the models, the only possible extra dimension allowed is 1. The points higher than 6 are understood as an overflow, given that we did not simulate any events with higher than $n = 6$.

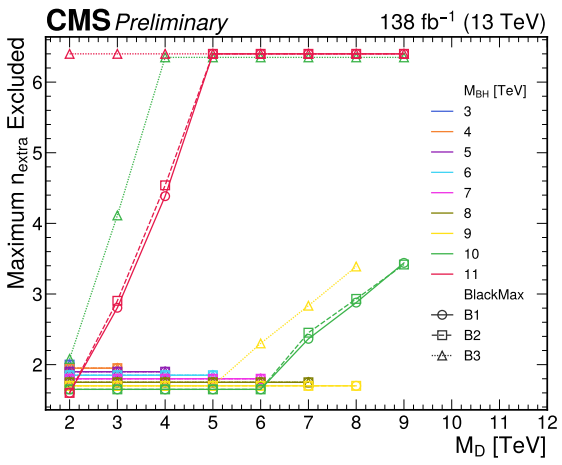

FIGURE 9: The maximum number of excluded extra dimensions as a function of M_D, M_{BH} values for the BLACKMAX models. The points seen near n_{extra}^{max} values of 2 and 6 are to be understood as underflow and overflow values given the simulation parameter choices at $n = 2, 4, 6$.

The last interpretation is on the sphalerons. Figure 10 shows the observed limits on the pre-exponential factor for the sphaleron models with $p(N_{CS}) = 0$, 0.5 and 1 as a function of the sphaleron transition energy.

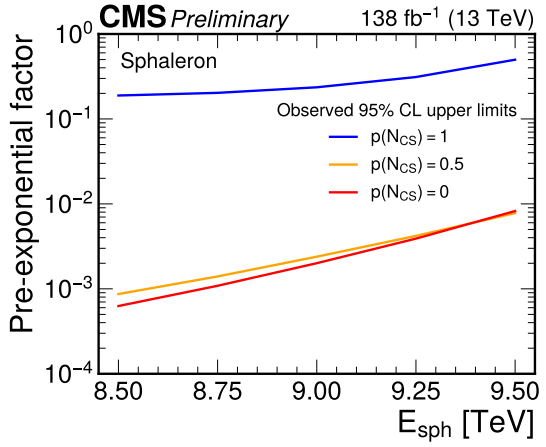

FIGURE 10: Observed limits on the pre-exponential factor for the sphaleron models with $p(N_{CS}) = 0.0$, 0.5 and 1.

9. SUMMARY

We presented a new method for representing collision data and utilized advanced machine learning tools to distinguish signals from background in the search for black holes and sphalerons at the LHC, using 138 fb^{-1} of data collected by the CMS detector at a center-of-mass energy of 13 TeV. We excluded microscopic black holes with masses below 9.0−11.4 TeV, depending on the Plank scale, extending previous exclusions by 1−1.6 TeV. We also interpreted the results as an exclusion on the number of extra dimensions within these models, assuming a range of black hole masses and Planck scales. We presented limits on the sphaleron pre-exponential factor to be 5×10^{-4} to 2×10^{-3}, which is a 10-fold increase with respect to the past results.

References

[1] Karl Schwarzschild. On the gravitational field of a mass point according to Einstein's theory. *Sitzungsber. Preuss. Akad. Wiss. Berlin (Math. Phys.)*, 1916:189–196, 1916.

[2] Ignatios Antoniadis, Nima Arkani-Hamed, Savas Dimopoulos, and G. R. Dvali. New dimensions at a millimeter to a Fermi and superstrings at a TeV. *Phys. Lett. B*, 436:257, 1998.

[3] Nima Arkani-Hamed, Savas Dimopoulos, and G. R. Dvali. The Hierarchy problem and new dimensions at a millimeter. *Phys. Lett. B*, 429:263, 1998.

[4] Nima Arkani-Hamed, Savas Dimopoulos, and G. R. Dvali. Phenomenology, astrophysics and cosmology of theories with submillimeter dimensions and TeV scale quantum gravity. *Phys. Rev. D*, 59:086004, 1999.

[5] Lisa Randall and Raman Sundrum. An Alternative to compactification. *Phys. Rev. Lett.*, 83:4690, 1999.

[6] Lisa Randall and Raman Sundrum. A Large mass hierarchy from a small extra dimension. *Phys. Rev. Lett.*, 83:3370, 1999.

[7] Savas Dimopoulos and Greg L. Landsberg. Black holes at the LHC. *Phys. Rev. Lett.*, 87:161602, 2001.

[8] Steven B. Giddings and Scott D. Thomas. High-energy colliders as black hole factories: The end of short distance physics. *Phys. Rev. D*, 65:056010, 2002.

[9] Aurora Singstad Grefsrud, Trygve Buanes, Fotis Koutroulis, Anna Lipniacka, Rafal Maselek, Andreas Papaefstathiou, Kazuki Sakurai, Therese B. Sjursen, and Igor Slazyk. Machine learning classification of sphalerons and black holes at the LHC. *Eur. Phys. J. C*, 84(4):442, 2024.

[10] CMS Collaboration. The CMS experiment at the CERN LHC. *JINST*, 3:S08004, 2008.

[11] CMS Collaboration. Search for microscopic black holes and sphalerons in proton-proton collisions at 13 TeV, 2025. Physics Analysis Summary, CMS-PAS-EXO-24-028.

[12] Gerard 't Hooft. Symmetry Breaking Through Bell-Jackiw Anomalies. *Phys. Rev. Lett.*, 37:8, 1976.

[13] Frans R. Klinkhamer and N. S. Manton. A Saddle Point Solution in the Weinberg-Salam Theory. *Phys. Rev. D*, 30:2212, 1984.

[14] S. H. Henry Tye and Sam S. C. Wong. Bloch Wave Function for the Periodic Sphaleron Potential and Unsuppressed Baryon and Lepton Number Violating Processes. *Phys. Rev. D*, 92(4):045005, 2015.

[15] John Ellis and Kazuki Sakurai. Search for Sphalerons in Proton-Proton Collisions. *JHEP*, 04:086, 2016.

[16] Andreas Papaefstathiou, Simon Plätzer, and Kazuki Sakurai. On the phenomenology of sphaleron-induced processes at the LHC and beyond. *JHEP*, 12:017, 2019.

[17] Andreas Ringwald, Kazuki Sakurai, and Bryan R. Webber. Limits on Electroweak Instanton-Induced Processes with Multiple Boson Production. *JHEP*, 11:105, 2018.

[18] De-Chang Dai, Glenn Starkman, Dejan Stojkovic, Cigdem Issever, Eram Rizvi, and Jeff Tseng. BlackMax: A black-hole event generator with rotation, recoil, split branes, and brane tension. *Phys. Rev. D*, 77:076007, 2008.

[19] C. M. Harris, P. Richardson, and B. R. Webber. CHARYBDIS: A Black hole event generator. *JHEP*, 08:033, 2003.
[20] James A. Frost, Jonathan R. Gaunt, Marco O. P. Sampaio, Marc Casals, Sam R. Dolan, Michael Andrew Parker, and Bryan R. Webber. Phenomenology of Production and Decay of Spinning Extra-Dimensional Black Holes at Hadron Colliders. *JHEP*, 10:014, 2009.
[21] S. Creek, O. Efthimiou, P. Kanti, and K. Tamvakis. Greybody factors for brane scalar fields in a rotating black-hole background. *Phys. Rev. D*, 75:084043, 2007.
[22] S. Creek, O. Efthimiou, P. Kanti, and K. Tamvakis. Scalar Emission in the Bulk in a Rotating Black Hole Background. *Phys. Lett. B*, 656:102, 2007.
[23] Hirotaka Yoshino and Vyacheslav S. Rychkov. Improved analysis of black hole formation in high-energy particle collisions. *Phys. Rev. D*, 71:104028, 2005. [Erratum: Phys.Rev.D 77, 089905 (2008)].
[24] Benjamin Koch, Marcus Bleicher, and Sabine Hossenfelder. Black hole remnants at the LHC. *JHEP*, 10:053, 2005.
[25] Horst Stoecker. Stable TeV - Black Hole Remnants at the LHC: Discovery through Di-Jet Suppression, Mono-Jet Emission and a Supersonic Boom in the Quark-Gluon Plasma. *Int. J. Mod. Phys. D*, 16:185, 2007.
[26] Fabio Scardigli. Glimpses on the micro black hole Planck phase. *Symmetry*, 12(9):1519, 2020.
[27] Savas Dimopoulos and Roberto Emparan. String balls at the LHC and beyond. *Phys. Lett. B*, 526:393, 2002.
[28] Douglas M. Gingrich and Kevin Martell. Study of highly-excited string states at the Large Hadron Collider. *Phys. Rev. D*, 78:115009, 2008.
[29] Cameron Bravo and Jay Hauser. BaryoGEN, a Monte Carlo Generator for Sphaleron-Like Transitions in Proton-Proton Collisions. *JHEP*, 11:041, 2018.
[30] R. Frederix, S. Frixione, V. Hirschi, D. Pagani, H. S. Shao, and M. Zaro. The automation of next-to-leading order electroweak calculations. *JHEP*, 07:185, 2018. [Erratum: JHEP 11, 085 (2021)].
[31] J. Alwall, S. Hoche, F. Krauss, N. Lavesson, L. Lonnblad, F. Maltoni, M. L. Mangano, M. Moretti, C. G. Papadopoulos, F. Piccinini, S. Schumann, M. Treccani, J. Winter, and M. Worek. Comparative study of various algorithms for the merging of parton showers and matrix elements in hadronic collisions. *Eur. Phys. J. C*, 53:473, 2008.
[32] Albert M Sirunyan et al. Extraction and validation of a new set of CMS PYTHIA8 tunes from underlying-event measurements. *Eur. Phys. J. C*, 80(1):4, 2020.
[33] Andrew J. Larkoski and Tom Melia. Covariantizing phase space. *Phys. Rev. D*, 102(9):094014, 2020.
[34] Tianji Cai, Junyi Cheng, Nathaniel Craig, Giacomo Koszegi, and Andrew J. Larkoski. The phase space distance between collider events. *JHEP*, 09:054, 2024.
[35] Corinna Cortes and Vladimir Vapnik. Support-vector networks. *Machine Learning*, 20(3):273, 1995.
[36] John Platt and Nikos Karampatziakis. Probabilistic outputs for svms and comparisons to regularized likelihood methods. 2007.
[37] Giovanni Punzi. Sensitivity of searches for new signals and its optimization. *eConf*, 030908:MODT002, 2003.
[38] Richard D. Ball et al. Parton distributions from high-precision collider data. *Eur. Phys. J. C*, 77(10):663, 2017.